Revista Internacional de Métodos Numéricos para Cálculo y Diseño en Ingeniería

ARTICLE

A Deep Learning-Based Time-Depth Conversion Method for Continuous Wellbore Temperature Profile Construction Using a Micro-Measurer

Mu Li[1,2], Yuxi Wang[2], Xianzhi Song[3], Shiming Duan[2], Hao Wang[2], Weiwei Hao[2] and Jiangshuai Wang[4,*]

[1]College of Artificial Intelligence, China University of Petroleum-Beijing, Beijing, China
[2]CNPC Engineering Technology R&D Company Limited, Beijing, China
[3]College of Petroleum Engineering, China University of Petroleum-Beijing, Beijing, China
[4]School of Petroleum and Natural Gas Engineering, Changzhou University, Changzhou, China
*Corresponding Author: Jiangshuai Wang. Email: wjs125126@163.com

Received: 27 February 2026; Accepted: 24 April 2026

ABSTRACT: Real-time monitoring of oil-gas wellbore temperature profiles provides important support for drilling strategy adjustment and model parameter calibration. MEMS-based micro-measurers can collect full-wellbore temperature data by flowing with drilling fluid circulation, but converting their time-series records to well depth relies on idealized steady-motion assumptions that neglect wall collisions, sticking, and local flow disturbances, introducing systematic positioning errors. In this study, a deep learning-based time-depth conversion method is proposed. A gated recurrent unit (GRU)-based temporal neural network is developed to extract motion-state features from six-axis dynamic signals, and a bounded velocity correction mechanism is introduced to compensate deviations from the idealized terminal velocity. The results show that: (1) The proposed model effectively learns motion-state deviations from dynamic response data and provides stable velocity correction under complex downhole conditions. (2) The corrected time-velocity curve exhibits transient fluctuations relative to the idealized terminal velocity, accurately capturing non-ideal behaviors while preserving directional stability. (3) During model training, the loss function decreases progressively and stabilizes, indicating good convergence and training stability. (4) Comparative analysis shows that the proposed GRU-Full method achieves a mean absolute anchor-point error of 1.23 m (0.24% of the well depth), outperforming the MLP and LSTM alternatives. Ablation experiments confirm that both the physical constraints and regularization terms contribute substantially to the model accuracy. This study enhances the spatial mapping accuracy of temperature data acquired by micro-measurers under complex downhole dynamic conditions. The established physically constrained deep learning framework provides a new technical pathway for refined wellbore thermal-field characterization and intelligent drilling decision-making.

KEYWORDS: Micro-measurer; wellbore temperature monitoring; wellbore temperature profile construction; dynamic response; deep learning; field test

1 Introduction

As oil and gas exploration continues to advance, downhole temperature and pressure conditions become increasingly severe, resulting in downhole complications such as kicks and losses [1–3]. Detailed analysis of drilling fluid properties and accurate identification of downhole complications require continuous monitoring of the wellbore temperature profile [4]. Such monitoring enhances well-control safety and improves operational efficiency.

Measurement-while-drilling [5] (MWD) tools are widely used in drilling operations. These tools enable real-time measurement of multiple engineering parameters, including temperature, pressure, torque, weight on bit, and vibration [6–8]. However, limitations in measurement point quantity and installation location restrict these tools to discrete depth responses, making them inadequate for continuous wellbore profile construction.

To enable continuous measurement of temperature data at different wellbore depths during drilling, Yu et al. [9] developed a downhole micro measurement device named "Microchip". This device incorporates MEMS-based sensing and data processing components within a $\phi 10\ \mathrm{mm}$ high-density polymer capsule, enabling autonomous acquisition of temperature and pressure data under confined wellbore conditions. During operation, the Microchip flows as circulation of drilling fluid through the drillstring, bit nozzles, and wellbore annulus, and ultimately returns the recorded data to the surface. Subsequent field deployments by Shi et al. [10] and Li et al. [11] in Saudi Arabia and Sichuan, China, validated the operational feasibility of this technology under actual drilling conditions. Following this effort, CNPC [12,13] and Sinopec [14–16] advanced the technology by developing measurement tools "micro-measurer" and "MSBs", promoting its transition from laboratory research to field pilot applications.

However, methods for constructing wellbore temperature profiles using a micro-measurer remain underdeveloped. The limited internal volume prevents integration of a high-precision real-time positioning module. The collected time-series data therefore cannot be directly correlated with well depth. Existing time-depth mapping and conversion methods are generally based on an assumption of idealized steady motion of the micro-measurer [17]. This assumption neglects complex dynamic behaviors in real wellbore environments such as wall collisions, sticking, and local flow disturbances, leading to limitations in practical engineering applications. Although magnetic-ring-based depth positioning has been validated in laboratory tests, the high implementation cost restricts its deployment in field operations.

In summary, although micro-measurers enable continuous wellbore temperature monitoring, the absence of a reliable time-depth conversion mechanism limits further improvements in profile accuracy. This limitation has become a key bottleneck restricting the accuracy of wellbore temperature profile construction. Accurately characterizing the motion dynamics of the micro-measurer in complex wellbore environments, while avoiding significant increases in operational cost, remains a critical challenge for achieving high-precision time-depth conversion.

In recent years, machine learning and deep learning techniques have been increasingly applied to various drilling engineering problems, including rate of penetration prediction [18], downhole temperature estimation [19], and proxy modeling for complex physical processes [20]. Recurrent neural network architectures, particularly long short-term memory (LSTM) and gated recurrent unit (GRU) networks, have demonstrated strong capability in capturing temporal dependencies within sequential drilling data [21]. Meanwhile, the concept of physics-informed machine learning has gained growing attention in subsurface engineering. Physics-informed neural networks (PINNs) integrate governing equations as soft constraints into the training process, and have been successfully applied to wellbore temperature prediction [22] and reservoir simulation with sparse data [23]. A comprehensive review by Latrach et al. [24] highlighted the increasing adoption of physics-constrained data-driven methods across geoscience, drilling, and reservoir engineering domains. However, most existing studies focus on predicting measurable physical quantities (e.g., temperature, pressure, or penetration rate) using labeled field or simulation data, whereas the time-depth conversion problem addressed in this study involves estimating an unobservable positional trajectory from indirect dynamic signals, with no labeled depth data available during the micro-measurer's downhole transit. This fundamental difference in problem formulation limits the direct applicability of conventional supervised or physics-informed learning frameworks.

To address these challenges, this study carries out development from both the hardware design and data-processing algorithm perspectives. Compared with conventional data-driven time-series prediction methods that rely solely on labeled training data, the proposed method integrates physics-based motion constraints directly into the learning process. The bounded velocity correction mechanism ensures physical interpretability of the network output, and the multi-component loss function encodes domain-specific constraints into the training process. This physics-constrained design distinguishes the present work from both purely empirical deep learning methods and classical analytical methods. The key contributions are summarized as follows:

(1) A micro-measurer integrating the measurement of temperature, pressure, and dynamic signals is developed, enabling continuous downhole temperature monitoring with the acquisition of related dynamic responses.
(2) A motion-state-aware time-depth conversion method is proposed, in which a recurrent neural network is used to learn motion-state features from recorded dynamic signals and to correct idealized motion assumptions for accurate positioning.
(3) Field tests are conducted to perform continuous monitoring and construction of the wellbore temperature profile. The reliability and effectiveness of both the micro-measurer and the proposed time-depth conversion method were verified.

This study provides an engineering-feasible solution for high-precision time-depth conversion of data acquired by micro-measurers. By incorporating motion-state awareness without increasing downhole system complexity, the method enhances the spatial mapping accuracy of wellbore temperature profiles. It further strengthens the capability for early detection of thermal anomalies and complex downhole conditions, thereby supporting safe and efficient development of deep and ultra-deep wells.

2 Downhole Multiphysics Micro-Measurer

2.1 System Composition

The micro-measurer serves as the primary device for continuous monitoring of wellbore temperature profiles. As illustrated in Fig. 1a, the micro-measurer is dropped into the drillstring after wireless activation, flows with the circulating drilling fluid through the bit nozzles, and then floats up in the wellbore annulus. Temperature and other physical parameters recorded at different wellbore depths are wireless transmitted to the host computer for subsequent data analysis.

As the micro-measurer is designed to work in confined downhole conditions, its hardware design integrates a variety of MEMS components and is organized into three subsystems, as shown in Fig. 1b.

The kernel system integrates a microcontroller unit, a Flash memory, and data interfaces supporting wireless/wired communication. The system measures, filters, amplifies, and stores the data in the 16 MB Flash memory, and supports data exchange with the host computer.

The power supply system consists of a button battery, a DC–DC converter, and a wireless charging module. External energy is received through an inductive coil and converted by the wireless charging circuitry into a charging voltage for the battery. The battery output is then regulated by a DC-DC converter to provide stable operating voltages for the micro-measurer.

The sensing system integrates temperature, pressure, and inertial sensors, enabling measurement of wellbore temperature and pressure, as well as the micro-measurer’s three-axis acceleration and three-axis angular velocity.

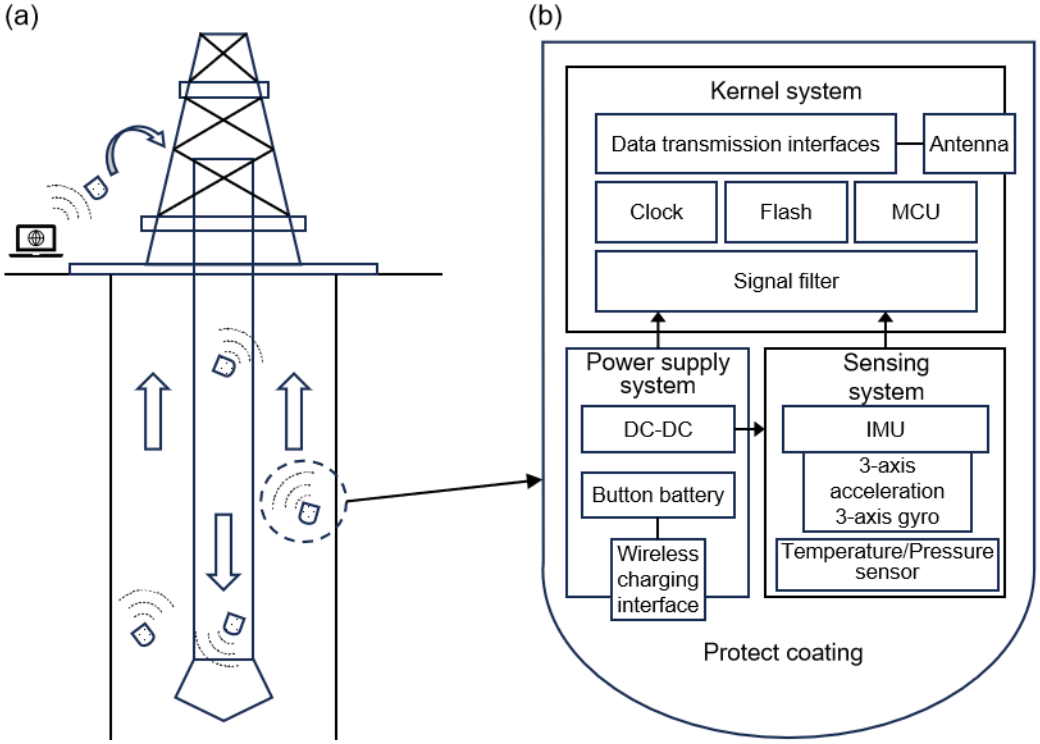

Figure 1: (**a**) Workflow of the micro-measurer; (**b**) System composition of the micro-measurer.

2.2 Hardware Design

As shown in Fig. 2a, the micro-measurer will integrate all system modules within a remarkably small size of $14\times\phi 10\ \mathrm{mm}$ bullet-shaped capsulation (Previous studies have demonstrated that the bullet-shaped design has superior hydrodynamic properties [25]). Given that the micro-measurer is required to circulate with the drilling fluid for more than 20 h while continuously acquiring wellbore physical parameters, the kernel circuit is designed to be compact and energy efficient. A low-power system-on-chip [26] (SoC) is selected as the control core, and a P-channel MOSFET load switch is used to enable dynamic power management [27] at runtime. All functional components are integrated into a four-layer printed circuit board, as shown in Fig. 2b.

The micro-measurer adopts an aerogel-epoxy composite encapsulation structure, its manufacturing process is shown in Fig. 2c. The circuit board is first wrapped with silicon-based aerogel for thermal insulation, then placed together with other components into a bullet-shaped mold. Liquid epoxy resin is poured into the mold and cured through a controlled thermal process to form the final encapsulated structure. The aerogel is composed of a high porosity nanostructure network [28] and exhibits a thermal conductivity lower than $0.035\ \mathrm{W/(m\cdot K)}$, thereby suppressing heat transfer between the drilling fluid and the circuit board. The cured epoxy features a bulk modulus of $2\sim4\ \mathrm{GPa}$ [29], enhancing the pressure and corrosion resistance of the micro-measurer. The fully encapsulated micro-measurer was subjected to laboratory high-temperature and high-pressure tests, which demonstrated stable operation for up to $20\ \mathrm{h}$ under temperatures of $160\ ^\circ\mathrm{C}$ and pressures of $160\ \mathrm{MPa}$.

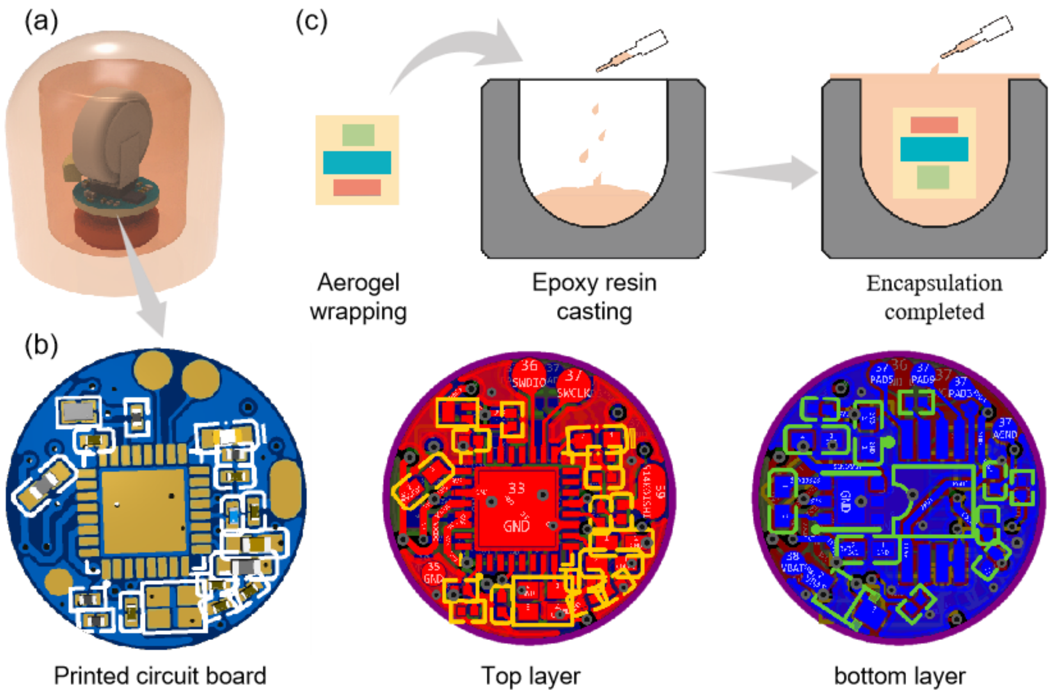

Figure 2: (**a**) Structure of the micro-measurer; (**b**) Circuit board design; (**c**) Manufacturing process.

3 Time-Depth Conversion Method

3.1 Motion Model of the Micro-Measurer

The axial motion of the micro-measurer is similar to the cuttings migration [30], and can be approximated as a one-dimensional problem. As shown in Fig. 3, the well depth direction is defined as the axial coordinate Z_{I}. The motion of the micro-measurer is governed by four principal forces acting along the well depth direction: gravity F_g, buoyancy F_{b}, drag $F_{\mathrm{D}}(v)$, and friction $F_{\mathrm{w}}(t)$ in the fluid. The governing equation of motion is formulated as Eq. (1):

$$m\frac{\mathrm{d}v}{\mathrm{d}t}=F_g-F_{\mathrm{b}}-F_{\mathrm{D}}(v)-F_{\mathrm{w}}(t) \tag{1}$$

where, v denotes the axial motion velocity of the micro-measurer, which is a function of time. Gravity and buoyancy are depicted in Eqs. (2) and (3):

$$F_g=mg \tag{2}$$

$$F_{\mathrm{b}}=\rho_{\mathrm{f}}gV \tag{3}$$

where, m and V are the mass and volume of the micro-measurer, ρ_{f} is the density of the drilling fluid.

The fluid drag force can be expressed by a quadratic drag model [31]:

$$F_{\mathrm{D}}(v)=\frac{1}{2}\rho_{\mathrm{f}}C_{\mathrm{D}}A\,|\,v-v_f\,|\,(v-v_f) \tag{4}$$

where, A denotes the flow area of the micro-measurer, v_f is the flow velocity of the fluid. C_{D} represents the drag coefficient, which is determined from the empirical correlation proposed by Zhang et al. [32]. This drag-coefficient correlation was developed for particle transport in drilling-related confined-flow environments, which is closer to the present wellbore transport scenario than free-settling correlations. It provides an explicit Reynolds-number-dependent expression that is convenient for section-wise terminal-velocity calculation.

$$Re_{\mathrm{P}} = \frac{d(v - v_f)\rho_{\mathrm{f}}}{\mu} \tag{5}$$

$$C_{\mathrm{D}} = \frac{24}{Re_{\mathrm{P}}}(1 + 0.173 Re_{\mathrm{P}}^{0.657}) + \frac{0.413}{1 + 16{,}300 Re_{\mathrm{P}}^{-1.09}} \tag{6}$$

where, Re_{P} denotes the particle Reynolds number, μ represents the dynamic viscosity of the drilling fluid, and d is the equivalent diameter of the micro-measurer.

The effects of wall contact and friction can be equivalently expressed as:

$$F_{\mathrm{w}}(v) = \mu_{\mathrm{w}} N(t)\,\mathrm{sgn}(v) \tag{7}$$

where, $N(t)$ means the normal contact force between the micro-measurer and the wellbore, μ_{w} is the equivalent friction coefficient.

As the intensity and location of wall contact are unobservable from the measurements, the friction term expressed in Eq. (7) is not resolvable within the micro-measurer motion model. The unmodeled friction effects will be addressed by the data-driven correction described in Section 3.2. In addition, due to its small mass and size, the micro-measurer rapidly reaches a stable flow velocity under the hydrodynamic forces exerted by the drilling fluid. Based on these two considerations, the idealized motion assumptions are applied to Eq. (1): The axial friction term is neglected, and the effect of transient acceleration on the time-depth conversion is ignored. The simplified governing equation is expressed as:

$$(m - \rho_{\mathrm{f}} V)g = \frac{1}{2}\rho_{\mathrm{f}} C_{\mathrm{D}} A \,|\, v_{\infty} - v_f \,|\, (v_{\infty} - v_f) \tag{8}$$

where, v_{∞} is the terminal velocity of the micro-measurer under the idealized motion assumption.

Under the idealized motion assumptions, the terminal flow velocity in each well section and the well depth $Z(t)$ should satisfy:

$$Z(t) = \int_0^t v_{\infty} d\tau \tag{9}$$

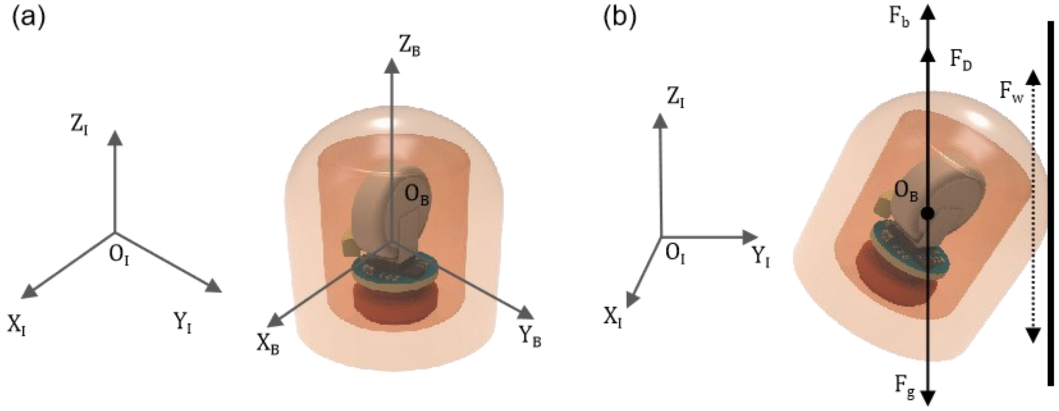

Figure 3: (**a**) Coordinate system definition; (**b**) Force analysis of the micro-measurer.

3.2 A Deep-Learning-Based Velocity Correction Model Driven by Dynamic Responses

Previous laboratory tests identified the six-axis IMU can effectively detect the vibration conditions of micro-measurers based on obvious variations of both the vibration amplitude and frequency of the micro-measurer in different downhole multiphase flow circumstances. The dynamic data measured by the IMU consists of acceleration $a(t)=[a_x(t),a_y(t),a_z(t)]$ and angular velocity $\omega(t)=[\omega_x(t),\omega_y(t),\omega_z(t)]$. The acceleration and angular velocity magnitude are used to characterize the dynamic energy of the micro-measurer.

$$a_{\mathrm{m}}(t)=\|a(t)\|=\sqrt{a_x^2+a_y^2+a_z^2} \tag{10}$$

$$\omega_{\mathrm{m}}(t)=\|\omega(t)\|=\sqrt{\omega_x^2+\omega_y^2+\omega_z^2} \tag{11}$$

Furthermore, the root mean square (RMS) and standard deviation of the acceleration and angular velocity magnitude in a sliding window of length L are constructed:

$$\begin{cases} a_{\mathrm{RMS}}(t)=\sqrt{\dfrac{1}{L}\sum\limits_{k=t-L+1}^{t}a_{\mathrm{m}}^2(k)} \\ \omega_{\mathrm{RMS}}(t)=\sqrt{\dfrac{1}{L}\sum\limits_{k=t-L+1}^{t}\omega_{\mathrm{m}}^2(k)} \\ \sigma_a(t)=\sqrt{\dfrac{1}{L-1}\sum\limits_{k=t-L+1}^{t}(a_{\mathrm{m}}(k)-\bar{a}_{\mathrm{m}})^2} \\ \sigma_\omega(t)=\sqrt{\dfrac{1}{L-1}\sum\limits_{k=t-L+1}^{t}(\omega_{\mathrm{m}}(k)-\bar{\omega}_{\mathrm{m}})^2} \end{cases} \tag{12}$$

The above statistical features are concatenated with the original six-axis dynamic signals to form a feature vector. The vector is normalized to characterize the differences among distinct motion states of the micro-measurer, such as wall collision, sticking, and normal motion.

$$\mathrm{x}(t)=[a_{\mathrm{m}}(t),\omega_{\mathrm{m}}(t),a_{\mathrm{RMS}}(t),\omega_{\mathrm{RMS}}(t),\sigma_a(t),\sigma_\omega(t),a_x(t),a_y(t),a_z(t),\omega_x(t),\omega_y(t),\omega_z(t)] \tag{13}$$

$$\tilde{\mathrm{x}}(t)=\frac{\mathrm{x}(t)-\mu}{\sigma} \tag{14}$$

The actual motion velocity is defined as:

$$v = v_\infty + \Delta v(t) \tag{15}$$

where, a bounded correction $\Delta v(t)$ features the effects of wall collision, sticking, and flow regime variation:

$$\Delta v(t) = \alpha s(t)\tanh(u_t) \tag{16}$$

where, $\alpha \in (0, 1)$ is maximum correction ratio, u_t represents the degree of motion-state deviation of the micro-measurer, and $s(t)$ is a scaling function defined in Eq. (17):

$$s(t) = \max(|v_\infty|, v_{\min}) \tag{17}$$

where, $v_{\min}$ is the minimum velocity scale.

In this study, a gated recurrent unit (GRU)-based temporal neural network model [33] is developed to extract motion-state features from the dynamic response of the micro-measurer, and a fully connected layer is carried out to generate a scalar output for velocity correction. In the GRU model, a larger value of the update gate state z_t indicates the more information from the current neuron is retained, where W_z means the update gate weight:

$$z_t = \sigma(W_z[h_{t-1}, x_t]) \tag{18}$$

In the GRU model, a larger value of the reset gate state r_t indicates a higher degree of utilizing historical information, where W_r means the reset gate weight:

$$r_t = \sigma(W_r[h_{t-1}, x_t]) \tag{19}$$

The specific output of the current neuron is given by:

$$\overline{h}_t = \tanh(W[r_t \odot h_{t-1}, x_t]) \tag{20}$$

The output of the GRU network is given by:

$$h_t = (1 - z_t) \odot h_{t-1} + z_t \odot \overline{h}_t \tag{21}$$

A fully connected layer is used to map the extracted features to the motion-state deviation of the micro-measurer.

$$u_t = W_o h_t + b_o \tag{22}$$

3.3 Construction of the Wellbore Parameters Profile

The mapping relation between the micro-measurer motion velocity and well depth is defined in Eq. (23):

$$Z(t) = Z(t_0) + \int_{t_0}^{t} v\,d\tau \tag{23}$$

The well depth at time k is calculated in Eq. (24):

$$Z_k = Z_{k-1} + \frac{\Delta t}{2}(v_k + v_{k-1}),\ k = 0,\ 1,\ 2,\ \ldots,\ N \tag{24}$$

where, Δt is the sampling interval of the micro-measurer.

The time anchors include the pump-start circulation time t_{in}, the bottomhole arrival time t_{down}, the onset time of floating up t_{up}, and the wellbore exit time t_{out}. These anchors are identified from the measured data or field operations to reduce cumulative data drift. An event-anchor constraint $\mathcal{L}_{\mathcal{A}}$ is then formulated based on these anchors:

$$\mathcal{A} = \{(t_{in}, 0), (t_{down}, Z_{well}), (t_{up}, Z_{well}), (t_{out}, 0)\} \tag{25}$$

$$\mathcal{L}_{\mathcal{A}} = \sum_{(t_i, z_i)\in\mathcal{A}} \omega_i (Z(t_i) - Z_i)^2 \tag{26}$$

where, Z_{well} denotes the known well depth, ω_i means the weight assigned to each anchor. In addition, a physical constraint $\mathcal{L}_M$ is imposed based on the directional consistency between the downward and upward motion phases:

$$\mathcal{L}_M = \lambda_M \left(\frac{1}{|\Omega_d|}\sum_{t\in\Omega_d} \max(0, -v) + \frac{1}{|\Omega_u|}\sum_{t\in\Omega_u} \max(0, v)\right) \tag{27}$$

To prevent non-physical large velocity fluctuations during the bottom hovering, a velocity magnitude constraint term $\mathcal{L}_D$ is introduced:

$$\mathcal{L}_D = \lambda_D \left(\frac{1}{|\Omega_{dw}|}\sum_{t\in\Omega_{dw}} \max(0, |v| - v_{dw})\right) \tag{28}$$

A smoothness regularization [34] term $\mathcal{L}_S$ and a magnitude penalty term $\mathcal{L}_\Delta$ are introduced to prevent severe temporal oscillations of the correction term:

$$\mathcal{L}_S = \lambda_S \cdot \frac{1}{T-1}\sum_{k=2}^{T}\left(\frac{\Delta v_k - \Delta v_{k-1}}{\Delta t}\right)^2 \tag{29}$$

$$\mathcal{L}_\Delta = \lambda_\Delta \cdot \frac{1}{T}\sum_{k=1}^{T}(\Delta v_k)^2 \tag{30}$$

The total loss of training is formulated as:

$$\mathcal{L} = \mathcal{L}_{\mathcal{A}} + \mathcal{L}_M + \mathcal{L}_D + \mathcal{L}_S + \mathcal{L}_\Delta \tag{31}$$

In this framework, the physical model and the deep learning correction play complementary roles. The motion model established in Eqs. (1)–(8) captures the dominant force balance and provides the terminal velocity as a physically grounded baseline. The neural network learns only a bounded residual as defined in Eq. (16) to compensate for unmodeled effects, particularly the wall friction expressed in Eq. (7), which is not resolvable from measurements. The multi-component loss function ensures that the learned corrections remain physically plausible: Eq. (26) aligns the integrated depth with known wellbore geometry, Eq. (27) enforces directional consistency in each motion phase, Eq. (28) suppresses non-physical motion during bottom hovering, and Eqs. (29)–(31) regularize the temporal behavior of the correction term. This design prevents the network from producing arbitrary velocity profiles and constrains it to learn only the physically meaningful deviations that the analytical model cannot capture.

The complete procedure of the time-depth conversion is shown in Fig. 4:

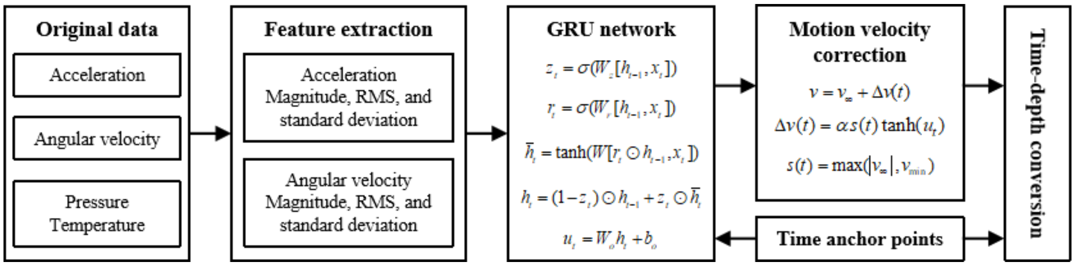

Figure 4: Time-depth conversion method workflow.

4 Results and Discussion

A field test for continuous monitoring of the wellbore temperature profile was conducted at an exploration well in Sichuan, China. The summary of field information is listed in Table 1.

Table 1: Summary of field information.

Parameter	Value
Well depth, m	502
Drill pipe ID/OD, in	4.276/5
Open hole diameter, in	6.5
Mud density (Mud weight), kg/m^3	1150
Dynamic viscosity, mPa·s	20
Mud type	WBM
Pump rate, L/s	50
Micro-measurer density, kg/m^3	1120
Micro-measurer diameter, mm	20

At 19:40 on the test day, 14 micro-measurers were deployed into the drillstring. The drilling pump was turned on at 19:45. Approximately 20 min after circulation started, Bluetooth signals were detected, and 6 micro-measurers with valid data were subsequently recovered at the shale shaker and flowline, achieving a 42.8% recovery success rate. All recovered devices contained complete and intact data records. The field test procedure is illustrated in Fig. 5a.

Prior to deployment, the micro-measurers were wirelessly activated and configured to sample at a frequency of 1 Hz. Throughout the circulation process, each device continuously recorded wellbore temperature along with its own three-axis acceleration and three-axis angular velocity. One of them with high data quality was selected for detailed analysis. The magnitudes of the acceleration and angular velocity were calculated as shown in Fig. 5b. The time anchors defined in Eq. (25) are identified through analysis of the amplitude, frequency, and fluctuation characteristics of the dynamic signals in conjunction with field operation records.

At 2255 s, circulation was initiated by activating the drilling pump, which drove the micro-measurer into motion within the drillstring. At 2459 s, oscillations and abrupt amplitude changes were observed, indicating that the micro-measurer moved through the bit nozzles with the drilling fluid flow. At 2644 s, the fluctuation frequency of the angular velocity decreased while the acceleration magnitude became relatively stable, suggesting that the micro-measurer started to float up in the annulus. At 3487 s, the micro-measurer was detected by the surface radio-frequency scanning system, and a wireless connection was established for data transmission. The micro-measurer was finally recovered at the drilling fluid trough.

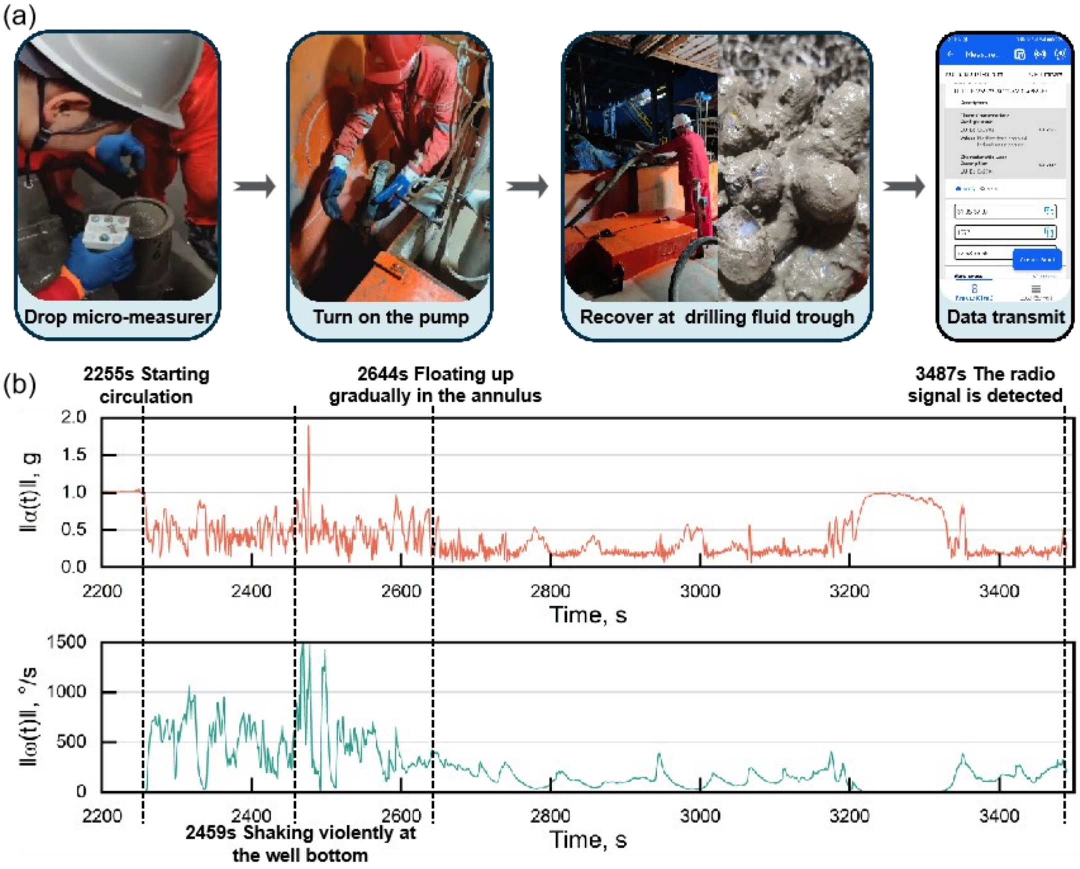

Figure 5: (**a**) Field test process; (**b**) The acceleration and angular velocity magnitude.

The wellbore temperature profile was constructed using the time-depth conversion method described in Section 3. The calculations in Eqs. (1)–(8) were performed based on the field parameters listed in Table 1, while the feature vector in Eq. (13) was constructed using the dynamic data measured by the IMU. The configuration of the GRU-based velocity correction model is summarized in Table 2. A lightweight single-layer GRU architecture is adopted because the network serves as a bounded residual corrector rather than an end-to-end predictor, and the training is performed on a single field trajectory with limited samples. These inputs were incorporated into the workflow shown in Fig. 4. In particular, the time anchors required in Eq. (25) were determined from the amplitude-frequency characteristics analysis described above.

Table 2: Configuration of the GRU-based velocity correction model.

Parameter	Value
Input feature dimension	12
GRU hidden size	64
GRU layers	1
Fully connected hidden dimension	32
Output dimension	1
Sliding window length (L), s	3
Maximum correction ratio (a)	0.6

Minimum velocity scale ($v_{\min}$), m/s	0.2
Optimizer	Adam
Learning rate	0.001
Training epochs	450
Loss weights (L_M , L_D , L_S , L_Δ)	25,25,0.8,0.5

Since no labeled depth data is available during downhole transit, the model is trained via self-supervised anchor alignment on the same trajectory, and the anchor-point errors reflect the optimization quality under physical constraints. To evaluate the proposed method, five model configurations are compared: a multilayer perceptron (MLP) without temporal modeling capability, a long short-term memory (LSTM) network as an alternative recurrent architecture [20], the proposed GRU with full physical constraints (GRU-Full), and two ablation variants, one without the directional consistency and dwell constraints in Eqs. (27) and (28) (GRU-NoPhy), and one without the smoothness and magnitude regularization in Eqs. (29) and (30) (GRU-NoReg). All five configurations share the same bounded velocity correction mechanism defined in Eq. (16) and the same training data.

Fig. 6a compares the depth trajectories produced by the five learning-based methods. All methods yield continuous and smooth depth profiles that pass close to the anchor points, confirming the effectiveness of the anchor-alignment loss in Eq. (26). Among them, GRU-Full achieves the closest alignment with the target anchor depths. During the downward stage, the depth increases monotonically with time. After reaching the bottomhole, the micro-measurer remains at an approximately constant depth for a short period. During the upward stage, the depth decreases monotonically with time.

Fig. 6b compares the terminal velocity $v_\infty(t)$ under the idealized motion assumption with the corrected velocity $v(t)$ predicted by the proposed GRU-Full model. In the downward stage, the corrected velocity exhibits transient fluctuations relative to the terminal velocity. These fluctuations are associated with wall collisions, eccentric motion, and local flow disturbances. During the upward stage, the corrected velocity varies smoothly and shows low-frequency behavior consistent with annular flow conditions. In both the downward and upward stages, the corrected velocity preserves the same motion direction as the terminal velocity, without sign reversal. This result confirms the effectiveness of the directional-consistency constraint.

Fig. 6c presents the anchor-point depth errors for all five methods, and the quantitative results are summarized in Table 3. As discussed in the preceding paragraph, the non-zero anchor residuals arise from the competing constraint terms. GRU-Full achieves the lowest mean absolute error (MAE) of 1.23 m, corresponding to a relative error of 0.24% with respect to the total well depth. In comparison, the LSTM and MLP methods yield MAEs of 3.43 m and 3.98 m, respectively. The ablation results further demonstrate the contribution of each constraint component: removing the physical constraints (GRU-NoPhy) increases the MAE to 3.49 m, and removing the regularization terms (GRU-NoReg) increases the MAE to 3.48 m. Both ablation variants degrade to a performance level comparable to LSTM, indicating that the physical constraints and regularization terms each contribute substantially to the accuracy of the proposed method.

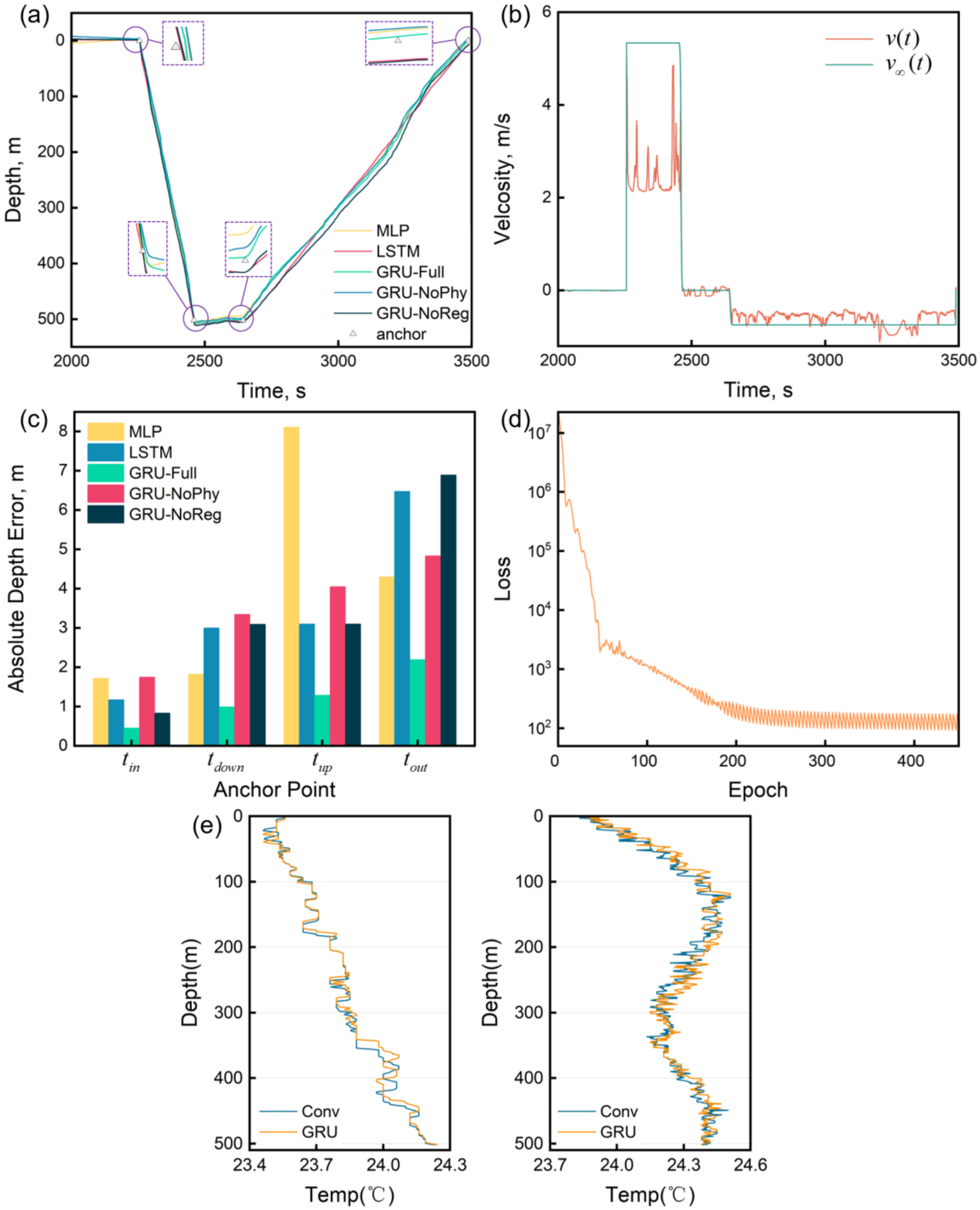

Figure 6: (**a**) Depth trajectory comparison of different model configurations; (**b**) Comparison between the terminal velocity and the corrected velocity; (**c**) Anchor-point depth errors; (**d**) Total loss; (**e**) Wellbore temperature profiles constructed by the conventional method and the proposed method.

Table 3: Anchor-point depth errors of different model configurations.

Method	E_{in}, **m**	E_{down}, **m**	E_{up}, **m**	E_{out}, **m**	**MAE, m**	**Rel.Error, %**
MLP	1.71	1.82	8.11	4.30	3.98	0.79
LSTM	1.71	2.99	3.10	6.47	3.43	0.68
GRU-Full	0.45	0.99	1.28	2.19	1.23	0.24

GRU-NoPhy	1.74	3.34	4.04	4.83	3.49	0.69
GRU-NoReg	0.83	3.09	3.10	6.89	3.48	0.69

Fig. 6d plots the total loss as a function of training epochs on a logarithmic scale. The total loss in Eq. (31) is a weighted combination of five constraint terms with heterogeneous physical dimensions, and its absolute magnitude is governed by the weighting coefficients rather than by prediction accuracy in physical units. The loss decreases rapidly during early iterations from 10^7 to 10^2, spanning five orders of magnitude, indicating effective convergence of all competing constraints toward a physically consistent solution. As training continues, the rate of decrease slows and the loss stabilizes while the motion-state correction term is refined.

Fig. 6e compares the wellbore temperature profiles constructed using the conventional method and the proposed GRU-Full method. Existing time-depth conversion methods typically calculate the terminal velocity from the idealized motion model in Eq. (8) and then rescale it within each motion phase to match the known time anchors, resulting in a piecewise-uniform velocity distribution. Such methods neglect the wall friction in Eq. (7) and other complex dynamic effects, and cannot resolve local velocity variations caused by wall collisions, sticking, or flow disturbances. Both methods produce consistent overall trends of temperature increasing with depth. At the same depth, temperatures measured during the upward stage are generally higher than those measured during the downward stage, which results from the longer heat-exchange duration of the annular fluid and the heat transfer between the annular fluid, the wellbore wall, and the formation [35-36]. However, the conventional method distributes temperature measurements evenly along the depth axis, resulting in spatially compressed profiles in regions where the micro-measurer decelerates. In contrast, the proposed method utilizes the dynamic response signals to identify local velocity variations, yielding a non-uniform depth allocation that better resolves the spatial distribution of the temperature field. The GRU-corrected profiles exhibit smoother depth-dependent gradients, which is more consistent with the expected continuous geothermal behavior in the wellbore.

5 Conclusions

This study addressed the time-depth conversion challenge for data collected by a circulation-based downhole micro-measurer. A motion-state-aware time-depth conversion framework was established by integrating physically constrained deep learning with dynamic-response sensing, enabling high-precision mapping between time-series measurements and wellbore depth. The results demonstrate that incorporating motion-state features effectively compensates for deviations from idealized motion assumption, reduces cumulative depth drift under complex downhole dynamic conditions, and significantly improves the construction accuracy of continuous wellbore temperature profiles.

The developed micro-measurer enables synchronized acquisition of temperature, pressure, and six-axis dynamic signals during drilling fluid circulation. Field tests confirmed the applicability of the measurement system and the time-depth conversion method under actual drilling conditions. The constructed temperature profiles are consistent across different motion stages and clearly distinguish the thermal distribution between the inner drillstring and the annulus.

Comparative analysis demonstrates that the proposed GRU-Full method achieves the lowest anchor-point depth error among all tested configurations, outperforming the MLP and LSTM alternatives under the same training framework. Ablation experiments further confirm that both the physical constraints and the regularization terms contribute substantially to accuracy, as removing either component increases the error to a level comparable to the LSTM baseline.

This study improves the data spatial mapping accuracy and engineering adaptability of micro-measurer technology in complex wellbore environments without increasing downhole system complexity. The results of this study can be utilized to support thermal anomaly detection and early identification of complex downhole conditions. It should be noted that the current validation is based on a single field test conducted at a 502 m vertical well with water-based mud. The generalizability of the proposed method to deeper wells, deviated or horizontal wellbores, and different mud systems (e.g., oil-based mud with different rheological properties) requires further investigation. In particular, the terminal velocity model and the drag coefficient correlation may need to be recalibrated for significantly different wellbore geometries or fluid properties. Nevertheless, the proposed framework is designed to be transferable. Specifically, the GRU-based residual correction structure, the bounded velocity mechanism, and the multi-component loss function are independent of specific well conditions and can be applied to new wells by updating the physical prior parameters and re-identifying the time anchors from the dynamic signal characteristics. Future work will focus on multi-well validation under diverse drilling conditions, enhance motion-state recognition and multi-physics parameter fusion modeling, validate the method across additional well types, and promote coordinated optimization of hardware and algorithms.

Acknowledgement: Not applicable.

Funding Statement: This paper was supported by the National Science and Technology Major Project (Grant No. 2025ZD1402000, No. 2025ZD1402004).

Author Contributions: The authors confirm contribution to the paper as follows: study conception and design: Mu Li, Yuxi Wang, Xianzhi Song, Shiming Duan; data collection: Hao Wang, Weiwei Hao; analysis and interpretation of results: Jiangshuai Wang; draft manuscript preparation: Mu Li, Yuxi Wang. All authors reviewed and approved the final version of the manuscript.

Availability of Data and Materials: The datasets generated during and/or analyzed during the current study are available from the corresponding author on reasonable request.

Ethics Approval: Not applicable.

Conflicts of Interest: The authors declare no conflict of interest.

References

1. Su YN, Lu BP, Liu YS, Zhou YC, Liu XS, Liu W, et al. Status and research suggestions on the drilling and completion technologies for onshore deep and ultra deep wells in China. Oil Drill Prod Technol. 2020;42(5):527–42. (In Chinese).
2. Wang HG, Huang HC, Ji GD, Chen CC, Lv ZH, Chen WF, et al. Progress and challenges of drilling and completion technologies for deep, ultra-deep and horizontal wells of CNPC. China Petrol Explor. 2023;28(3):1–11. (In Chinese).
3. An J, Li J, Huang H, Liu G, Yang H, Zhang G, et al. Mud loss behavior in fractured formation with high temperature and pressure. Energy Rep. 2023;9:2638–52. doi:10.1016/j.egyr.2023.01.080.
4. Zhao X, Zhao Y, Wang Z, Chen G, Li P, Liang W, et al. Wellbore temperature distribution during drilling of natural gas hydrate formation in South China Sea. Petroleum. 2021;7(4):451–9. doi:10.1016/j.petlm.2021.10.008.
5. Ward C, Andreassen E. Pressure-while-drilling data improve reservoir drilling performance. SPE Drill Complet. 1998;13(1):19–24. doi:10.2118/37588-pa.
6. Wang H, Huang H, Bi W, Ji G, Zhou B, Zhuo L. Deep and ultra-deep oil and gas well drilling technologies: Progress and prospect. Nat Gas Ind B. 2022;9(2):141–57. doi:10.1016/j.ngib.2021.08.019.
7. Su YN, Dou XR, Gao WK, Liu K. Discussion and prospects of the development on measurement while drilling technology in oil and gas wells. Petrol Sci Bull. 2023;8(5):535–54. (In Chinese).
8. Abbaszadeh Shahri A, Shan C, Larsson S, Johansson F. Normalizing large scale sensor-based MWD data: An automated method toward a unified database. Sensors. 2024;24(4):1209. doi:10.3390/s24041209.
9. Yu M, He S, Chen Y, Takach N, LoPresti P, Zhou S, et al. A distributed microchip system for subsurface measurement. In: SPE Annual Technical Conference and Exhibition; 2012 Oct 8–10; San Antonio, TX, USA. doi:10.2118/159583-ms.

10. Shi Z, Li B, Gooneratne C, Zhan GD. Wireless activated drilling microchip for wellbore temperature measurement. In: International Petroleum Technology Conference; 2020 Jan 13–15; Dhahran, Saudi Arabia. doi:10.2523/iptc-19985-ms.
11. Li B, Zhan G, Okot M, Dokhani V. Analysis of circulating pressure and temperature using drilling microchips. In: International Petroleum Technology Conference; 2023 Mar 1–3; Bangkok, Thailand. doi:10.2523/iptc-22805-ms.
12. Liu W, Liao ML, Li M, Zhu ZQ, Fu JS. A downhole multiphysics measuring device based on MEMS microchips. J China Univ Petrol Ed Nat Sci. 2023;47(3):87–95. (In Chinese).
13. Li M, Liu W, Zhang H, Tang C, Fu J, Zhai X, et al. Field test research on the downhole multiphysics micro-measurer based on the MEMS microchip. Front Earth Sci. 2023;11:1164839. doi:10.3389/feart.2023.1164839.
14. Zhu Z, Zhao J, Mulunjkar A, Rached R, Gramajo E, Li F, et al. Measurements during drilling through an innovative microchip technology to determine accurate wellbore properties for efficient drilling operations. In: SPE Annual Technical Conference and Exhibition; 2021 Sep 21–23; Dubai, United Arab Emirates. doi:10.2118/205899-ms.
15. Tella S, Li S, Li J, Zhan G. Reliability study of data microchips for downhole data acquisition subjected to pseudorandom vibrations. In: Abu Dhabi International Petroleum Exhibition and Conference; 2024 Nov 4–7; Abu Dhabi, United Arab Emirates. doi:10.2118/222029-ms.
16. Tella SA, Alsheikh A, Li S, Li J, Zhan G. Field trials review on drilling data microchips deployment, recovery, and data retention. In: International Petroleum Technology Conference; 2025 Feb 18–20; Kuala Lumpur, Malaysia. doi:10.2523/iptc-25092-ea.
17. Dokhani V, Li B, Gooneratne C, Zhan G, Moellendick TE, Shi Z. Evaluation of circulating temperature in wellbores using drilling microchips: Modeling and case studies. J Petrol Sci Eng. 2022;211:110129. doi:10.1016/j.petrol.2022.110129.
18. Tu B, Bai K, Zhan C, Zhang W. Real-time prediction of ROP based on GRU-informer. Sci Rep. 2024;14:2133. doi:10.1038/s41598-024-52261-7.
19. Khaled MS, Wang N, Ashok P, van Oort E. Downhole temperature estimation in geothermal wells using a deep learning model based on LSTM neural networks. In: IADC/SPE International Drilling Conference and Exhibition; 2024 Mar 5–7; Galveston, TX, USA. doi:10.2118/217749-ms.
20. Deng Q, Qi G, Jiang J, Yang D. Optuna-CNN based proxy model for calculation of perforating shock loads. Geoenergy Sci Eng. 2026;261:214439. doi:10.1016/j.geoen.2026.214439.
21. Cho K, van Merriënboer B, Gulcehre C, Bahdanau D, Bougares F, Schwenk H, et al. Learning phrase representations using RNN encoder–decoder for statistical machine translation. In: Proceedings of the 2014 Conference on Empirical Methods in Natural Language Processing (EMNLP); 2014 Oct 25–29; Doha, Qatar. p. 1724–34. doi:10.3115/v1/D14-1179.
22. Hiba M, Zerpa LE, Fallah A, Khaled MS. Physics-informed machine learning model for real-time downhole temperature monitoring in HPHT and geothermal drilling. In: SPE Annual Technical Conference and Exhibition; Oct 20–22; Houston, TX, USA. doi:10.2118/228003-ms.
23. Han JX, Xue L, Wei YS, Qi YD, Wang JL, Liu YT, et al. Physics-informed neural network-based petroleum reservoir simulation with sparse data using domain decomposition. Petrol Sci. 2023;20(6):3450–60. doi:10.1016/j.petsci.2023.10.019.
24. Latrach A, Malki ML, Morales M, Mehana M, Rabiei M. A critical review of physics-informed machine learning applications in subsurface energy systems. Geoenergy Sci Eng. 2024;239:212938. doi:10.1016/j.geoen.2024.212938.
25. Wang YX, Li M, Liao ML, Liu W, Li TR, Chávez JP, et al. Measurement while drilling of downhole engineering parameters by application of a newly designed micro-measurer. Petrol Sci. 2025;22(7):2905–19. doi:10.1016/j.petsci.2025.04.025.
26. Merino P, Mujica G, Señor J, Portilla J. A modular IoT hardware platform for distributed and secured extreme edge computing. Electronics. 2020;9(3):538. doi:10.3390/electronics9030538.
27. Khan H, Ud Din I, Ali A, Husain M. An optimal DPM based energy-aware task scheduling for performance enhancement in embedded MPSoC. Comput Mater Contin. 2023;74(1):2097–113. doi:10.32604/cmc.2023.032999.
28. Lei J, Zheng S, Han Z, Niu Y, Pan D, Liu H, et al. A brief review on the preparation and application of silica aerogel. Eng Sci. 2024;30:1214.
29. Jin FL, Li X, Park SJ. Synthesis and application of epoxy resins: A review. J Ind Eng Chem. 2015;29:1–11. doi:10.1016/j.jiec.2015.03.026.
30. Clark RK, Bickham KL. A mechanistic model for cuttings transport. In: SPE Annual Technical Conference and Exhibition; 1994 Sep 25–28; New Orleans, LA, USA. doi:10.2118/28306-ms.

31. Sarpkaya T. Force on a circular cylinder in viscous oscillatory flow at low Keulegan—Carpenter numbers. J Fluid Mech. 1986;165:61–71. doi:10.1017/s0022112086002999.
32. Zhang HL, Li GS, Xiao L, Yang CS. Study on the influence of the rotation of drill string on cuttings transportation in horizontal well. Sci Technol Eng. 2016;16(2):125–30. (In Chinese).
33. Dey R, Salem FM. Gate-variants of gated recurrent unit (GRU) neural networks. In: 2017 IEEE 60th International Midwest Symposium on Circuits and Systems (MWSCAS); 2017 Aug 6–9; Boston, MA, USA. p. 1597–600. doi:10.1109/MWSCAS.2017.8053243.
34. Stickel JJ. Data smoothing and numerical differentiation by a regularization method. Comput Chem Eng. 2010;34(4):467–75. doi:10.1016/j.compchemeng.2009.10.007.
35. Zhang H, Su Y, Liao M, Zhu Z, Zhang H, Li Z, et al. Thermal management of drilling fluids with phase change materials in ultra-high temperature wells. Appl Therm Eng. 2025;274:126601. doi:10.1016/j.applthermaleng.2025.126601.
36. Deng Q, Jiang J, Yang D, et al. Dynamic analysis and optimization of perforated tubing strings in deep-water wells under diverse operating conditions[J]. Ocean Engineering, 2025, 322. doi:10.1016/j.oceaneng.2025.120535